3D printing of bulk thermoelectric materials: laser powder bed fusion of N-type silicon germanium

Maxime Baudry, Guillaume Savelli, Guilhem Roux

To cite this version:

Maxime Baudry, Guillaume Savelli, Guilhem Roux. 3D printing of bulk thermoelectric materials: laser powder bed fusion of N-type silicon germanium. Materials Science and Engineering: B, 2023, 298, pp.116897. cea-04287122

HAL Id: cea-04287122
https://cea.hal.science/cea-04287122v1

Submitted on 15 Nov 2023

3D printing of bulk thermoelectric materials: laser powder bed fusion of N-type silicon germanium

Maxime Baudry[a]*, Guillaume Savelli[a], Guilhem Roux[a]

[a] *Univ. Grenoble Alpes, CEA, Liten, DTNM, 38000 Grenoble, France*

Abstract

Among Additive Manufacturing (AM) methods, Laser Powder Bed Fusion (L-PBF), also called Selective Laser Melting (SLM), is prevalent to printing complex metal parts in small and medium series. Recent studies in L-PBF processing develops the manufacturing of new materials, including thermoelectric (TE) materials. This study presents manufacturing of an N type $Si_{80}Ge_{20}$ powder by L-PBF. Silicon germanium alloy is a TE material intended for high temperature applications. It is the first time that this semiconductor material is studied by AM technology. Dense samples of various shapes and sizes were produced, and a first process window was identified. Structural analyses have been performed, highlighting good densification. Unfortunately, mechanical cracking occurs in all samples. TE properties were investigated on as built samples, displaying low values (ZT=0.11 at 600°C), due to poor electrical conductivity. Overall, these results show that L-PBF of silicon germanium is possible, which could open up its scope of applications.

Keywords: Laser processing, Powder metallurgy, Thermoelectricity, Additive Manufacturing, Rapid solidification, Silicon Germanium

---

* Corresponding author. Tel.: +33 4 38 78 28 07
E-mail address: maxime.baudry@cea.fr

1. Introduction

Global energy consumption has risen significantly for 50 years and is expected to rise in the decades to come. In addition, the need of alternative ways of producing electricity that are not relying on fossil fuels amplifies to face current environmental issues. Many methods to produce energy involves heat, and therefore heat losses. Thermoelectric materials are capable of producing electricity while under temperature differences (Seebeck effect), and can conversely create a heat flux while under current (Peltier effect). So, these materials present themselves as an environmentally friendly way to harvest energy from heat losses and other heat sources.

Thermoelectric power generation does not require moving parts, and involves only solid-state materials, which makes this method reliable and durable for producing electricity with low-maintenance. Currently, the main setback for Thermo-Electric Generators (TEG) is their efficiency [1,2]. TEG efficiency is highly dependent of TE figure of merit (*ZT*) of materials, defined by equation (1):

$$ZT = \frac{\sigma S^2}{\kappa} T \tag{1}$$

with T the temperature and σ, S and κ the electrical conductivity, Seebeck coefficient, and thermal conductivity respectively. Another weak point for TEG is their poor geometry variety. Current conventional methods of bulk TE material production such as hot pressing or Spark Plasma Sintering (SPS) allow only to produce planar TE modules [3]. Besides, heat or cold sources shapes are often curved, which does not allow optimal heat transfer between TE device and hot/cold sources. Moreover, these techniques involve a dicing step to shape the bulk material into legs, which produce many losses due to TE materials brittleness [4–8].

Additive manufacturing (AM) offers a new approach to produce TE materials, allowing a huge variety of shapes and design. Parts are directly produced with desired shape, and can easily be removed from the plate, which enables to avoid drawbacks of the dicing step. Furthermore, these techniques unlock new microstructures that could lead to enhance materials TE performances. For the last five years, additive manufacturing of TE materials was studied using various techniques such as Laser powder bed fusion (L-PBF), solution printing [9] or fused deposition modelling [10]. Among these AM methods, L-PBF shows the most promising TE properties [10] because it involves only TE materials, without the need to mix it with polymers, in an ink or a slurry.

El Desouki et al. were the first to introduce AM of TE materials, with their work on L-PBFof Bi_2Te_3 [11]. Then, more research on Bi_2Te_3 was carried out [6–8,12–18] and more specifically with the work of Qui et al. and Shi et al. exhibiting especially high *ZT* (reaching peak values of 1.1 and 1.3 at 43°C and 50°C respectively)[13,14]. Other TE materials were also recently studied such as Sb_2Te_3 [19], MnSi [20], or Mg_2Si [21], leading for instance to flexible TE composites [9] and tube-like TEG [22].

L-PBF is an emerging additive manufacturing technique mostly used to produce metal parts from Computer Aided Design (CAD) models using metallic powder (Figure 1). This technique is well suited to produce complex parts in small or medium production runs. The CAD model is sliced, and then the part is built layer by layer by adding a thin layer of powder melt locally following the shape of the CAD model. Cooling rates involved in this process are fast (up to 10^4 to 10^6 $K.s^{-1}$), and thermal gradients are mostly oriented along the Building Direction (BD), which results generally in very fine grain anisotropic microstructures [23–25].

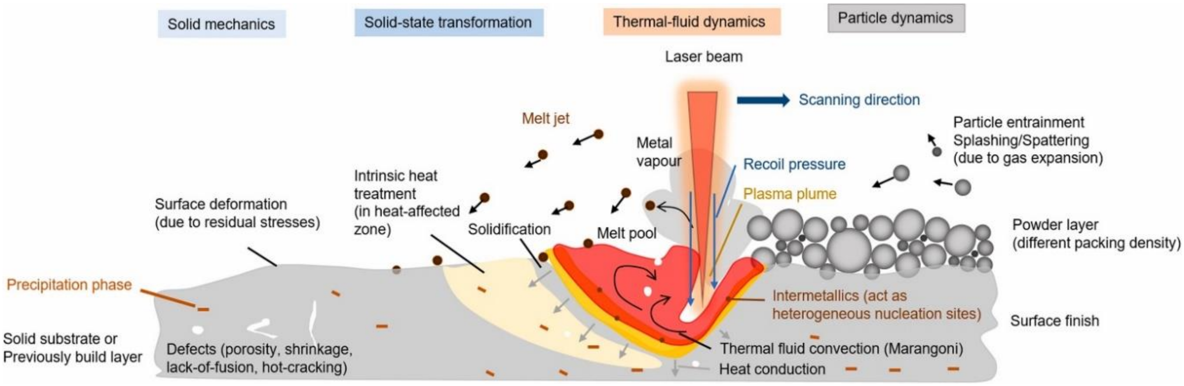

Figure 1. Schematic illustration of the Laser-Powder Bed Fusion (L-PBF) process showing the various phenomena induced by laser-powder interaction, solidification and solid-state transformation [26].

Silicon germanium SiGe is the most commonly used TE material for high temperature applications (800-1000°C) such as Radio Thermoelectric Generators (RTG) for satellites, or surveillance in hostile environments. SiGe alloy crystallizes in cubic diamond structure [27]. This structure is stable for all stoichiometries, with Ge atoms in substitution within the Si crystal. N-type SiGe can be easily obtained with phosphorus doping, while P-type can be obtained with boron, which enables producing TE devices with only one base material [2,5]. This work presents the development of L-PBF processing parameters in order to produce N-type SiGe parts, and characterization of the first SiGe samples produced via this process.

2. Materials and manufacturing methods

2.1. Powder properties

Figure 2 shows a SEM image of the N-SiGe powder used in this work, which was obtained by gas atomization. This image displays that a significant portion of particles exhibits low sphericity. A high number of small particles tends to group in clusters, or forms satellites around coarser particles, assuming strong static gripping. Table 1 presents results of powder chemical analysis by Inductively Coupled Plasma Optical Emission Spectroscopy (ICP-OES). Powder chemical composition is close to the common $Si_{80}Ge_{20}$ composition [2] with 1.2at.% phosphorus as doping element. Particle size distribution was measured with a laser scattering particle size distribution analyzer Master sizer 2000 from Malvern Instruments© (Table 2). Median particle size of the powder used is close to typical particle size for L-PBF (around 20µm). However, size repartition (d90%-d10%) is wide (55µm) compared to powders usually employed in L-PBF process (~25µm) [28] which corroborates SEM observations.

Morphologic analysis of powder particles was conducted thanks to image analysis software Morphologi. 50000 particles were detected by the software. Aggregates and particles that are too small to be analyzed by the software need to be excluded from the analysis, as they are not relevant. In this work, we first excluded particles with a diameter < 2µm (6054 particles excluded), and particles with solidity < 0.90 (1965 particles excluded).

41981 particles were retained for the final analysis. Particle aspect ratio (width / height) is presented in Table 2. This aspect ratio repartition is typical of particles with low sphericity, which corroborates SEM observations.

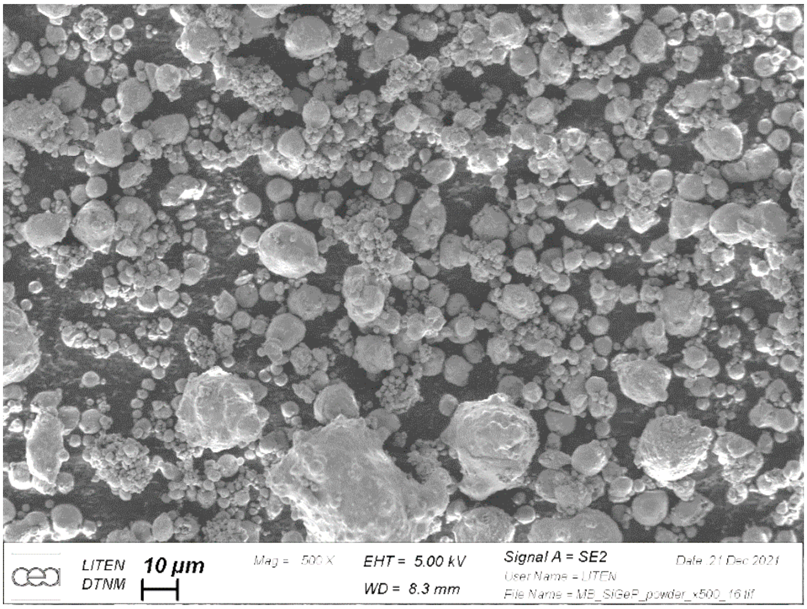

Figure 2. SEM image of N-SiGe powder used in this work.

Table 1. Chemical composition of N-SiGe powder measured par ICP-OES.

Atomic element	weight %	weight % uncertainty	atomic %	atomic % uncertainty
Silicon	61	3	79	2
Germanium	39	2	20	2
Phosphorus	1.0	0.1	1.2	0.1

Table 2. N-SiGe powder statistic repartition of particle size by volume and aspect ratio by number.

Size repartition (vol)	
d10%	4.7µm
d50%	16.3µm
d90%	60.2µm

Aspect ratio repartition (nb)	
First decile (10%)	0.66
Median (50%)	0.87
Last decile (90%)	0.96

Powder apparent density ρ_A and powder tapped density ρ_T were measured and compared according to standard 3923-2. Table 3 presents powder density and avalanche angle. Hausner ratio H_R and Carr index C_I are calculated respectively with equation (2) and (3) [29].

$$H_R = \rho_T / \rho_A \tag{2}$$

$$C_I = \frac{100\,(\rho_T - \rho_A)}{\rho_T} \tag{3}$$

Powder flowability can then be qualified with Hausner ratio and Carr index according to Table 4. Carr Index and Hausner ratio obtained for the powder used in this work indicate a very poor flowability, which is not ideal for a good powder spreading. Avalanche angle was measured with a revolution mercury scientific rotating drum. The powder is put in a drum, which rotates slowly [30]. Drum rotation will trigger avalanches that will be captured on camera. 200 avalanches are registered, and the avalanche angle value is the median of the 200 angles measured. Ideal avalanche angle for L-PBF is below 45°, in order to guarantee a good powder bed spreading. Avalanche angle measured for this powder is 55.8°, which confirms the bad flowability. Finally, photonic absorption at the laser wavelength (λ=1064nm) was measured by spectrophotometry with a Perkin Elmer Landa 950. Powder absorption measured at λ=1064nm is 85.3%, which is significantly higher than the typical value (60%) for metallic powders employed usually in L-PBF process. Powder pycnometer density was measured with an AccuPyc II 1340 Pycnometer. SiGe theoretical density can be calculated relative to Ge content in the material from [31] (3.008g.cm^{-3} for a $Si_{80}Ge_{20}$ composition). Pycnometer measurements yields 3.107g.cm^{-3}, slightly higher than theoretical value.

Overall, the N-SiGe powder used in this study is not optimal for L-PBF process, especially concerning its flowability characteristics, which will limit the choice of recoating systems usable for its spreading.

Table 3. N-SiGe powder flowability characteristics.

Powder characteristics	
Apparent density (g.cm^{-3})	1.219
Tapped density (g.cm^{-3})	1.824
Pycnometer density (g.cm^{-3})	3.107
Hausner ratio	1,50
Compressibility index	33,2
Avalanche angle	55,8°

Table 4. Powder flowability relative to Hausner ratio and Carr Index[29].

Flowability expected	Hausner ratio	Carr Index
Excellent / very free flow	1.00 – 1.11	< 10
Good / free flow	1.12 – 1.18	11 – 15
Fair	1.19 – 1.25	16 – 20
Passable	1.26 – 1.34	21 – 25
Cohesive / poor flow	1.35 – 1.45	26 – 31
Very cohesive / very poor flow	1.46 – 1.59	32 – 37
Approximately no flow	> 1.60	> 38

2.2. Printing parameters development

Printing parameters development was performed on a 3D systems ProX200 device, equipped with a 270W 1064nm wavelength laser with a 70µm spot diameter. ProX200 recoating system is a roller, which allows spreading powders with poor flowability. All productions in this work were conducted under argon atmosphere with a 1000ppm of dioxygen threshold, on a SAE 430 stainless steel plate support with a layer thickness value set to 30µm.

As there is no reference works of SiGe manufacturing by L-PBF, a study of single tracks stability with laser power ranging from 15W to 268W and laser speed ranging from 400 to 2000mm.s^{-1} was conducted. A printing quality map was drawn up (Figure 3) and displays a stable zone at speed ranging from 400mm.s^{-1} to 600mm.s^{-1} and laser power from 100W to 270W.

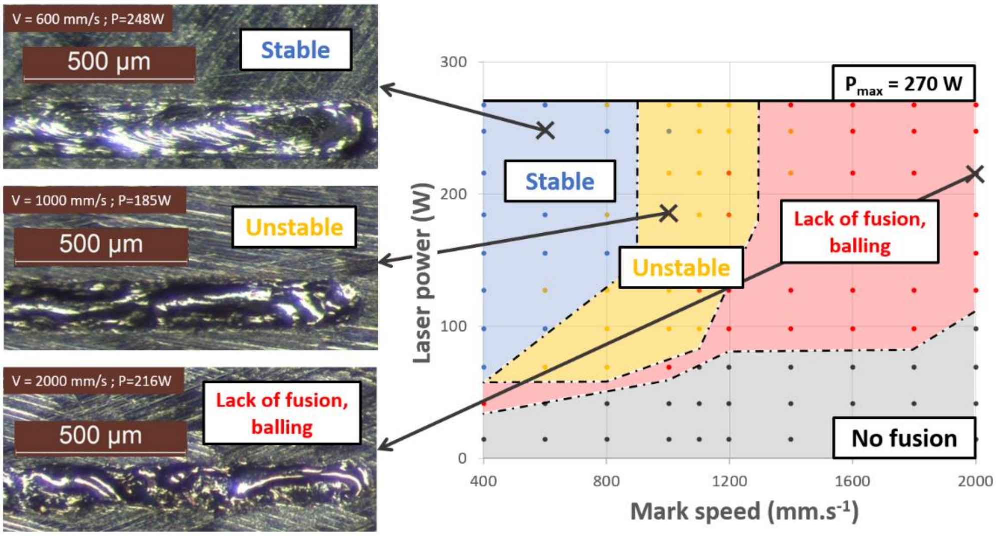

Figure 3. Printing quality map of N-SiGe single tracks with binocular images of the three groups identified.

The first attempt to build 3D parts with these stable parameters led to balling parts. Thermal behaviours are different between single tracks and 3D parts. SiGe thermal conductivity is low (4W.m^{-1}.K^{-1}) compared to regular alloys used in L-PBF (316L Steel: ~20W.m^{-1}.K^{-1} and AlSi$_7$: ~170W.m^{-1}.K^{-1}). As a result, heat accumulation occurs during 3D parts building, whereas in the case of single tracks, the steel tray quickly dissipates heat.

Therefore, a new lasing strategy is necessary to avoid heat accumulation and limit balling phenomenon while building 3D parts. The approach retained in this study is to give heat more time to dissipate by increasing the time between two laser tracks. To achieve this, the laser jump speed between two adjacent tracks was reduced from 5000mm.s^{-1} to 150mm.s^{-1}, in conjunction with a unidirectional scan strategy. This method led to successfully build 3D SiGe samples with various shapes, designed for TE properties characterisation.

Table 5 displays the eight sets of printing parameters that led to successfully build samples, on two trays. Their calculated volumic energy density *VED* is also presented. *VED* helps to draw qualitative comparison between different printing parameters sets, as it summarizes the combined effects of several L-PBF parameters. It is defined by equation 4 [32]:

$$VED = \frac{P}{t\,h\,v_{mark}} \tag{4}$$

with *P* the laser power, *t* the layer thickness, *h* the hatch, and v_{mark} the laser mark speed.

Table 5. Printing parameters that led to successfully build samples, with their calculated *VED*.

Printing parameters (Tray 1)	Set 1	Set 2	Set 3
Laser Power (W)	99	99	127
Mark speed (mm.s^{-1})	400	600	400
Volumic energy density (J.mm^{-3})	156	104	200
Jump speed (mm.s^{-1})	150	150	150
Hatch (µm)	45	45	45
Scan strategy	Unidirectional, 0-90°	Unidirectional, 0-90°	Unidirectional, 0-90°
Layer thickness (µm)	30	30	30

Printing parameters (Tray 2)	Set 4	Set 5	Set 6	Set 7	Set 8
Laser Power (W)	127	134	134	142	134
Mark speed (mm.s^{-1})	350	400	350	350	300
Volumic energy density (J.mm^{-3})	229	212	242	256	282
Jump speed (mm.s^{-1})	150	150	150	150	150
Hatch (µm)	45	45	45	45	45
Scan strategy	Unidirectional, 0-90°	Unidirectional, 0-90°	Unidirectional, 0-90°	Unidirectional, 0-90°	Unidirectional, 0-90°
Layer thickness (µm)	30	30	30	30	30

Table 6 displays samples printing quality relative to their shape, dimensions and printing parameters. Figure 4 shows top view of as built samples, alongside a general view of tray 2 (Figure 4a). Samples printed with set 1, and 3 to 6 show a smooth and uniform surface (Figure 4b, d-g). Printing parameters sets 3 to 6 displays also the best results in regards to printing quality. These four sets presents laser power ranging from 127 to 134W, laser speed ranging from 350 to 400mm.s^{-1} and *VED* ranging from 200 to 250J.mm^{-3}.

By contrast, set 2 sample (Figure 4c) display a large number of holes in its top surface. They were later found to be columnar defects aligned with BD. These are likely lack of fusion defects, as set 2 display high mark speed (600mm.s^{-1}) and low *VED* (104J.mm^{-3}) relative to other printing parameters sets. Some samples of set 7 and 8 display shinier areas on their top surface (Figure 4h, i). This surface state is also observed on cracked and overmelted parts, and is linked to the fact that both sets are the ones with the highest *VED* (>250J.mm^{-3}).

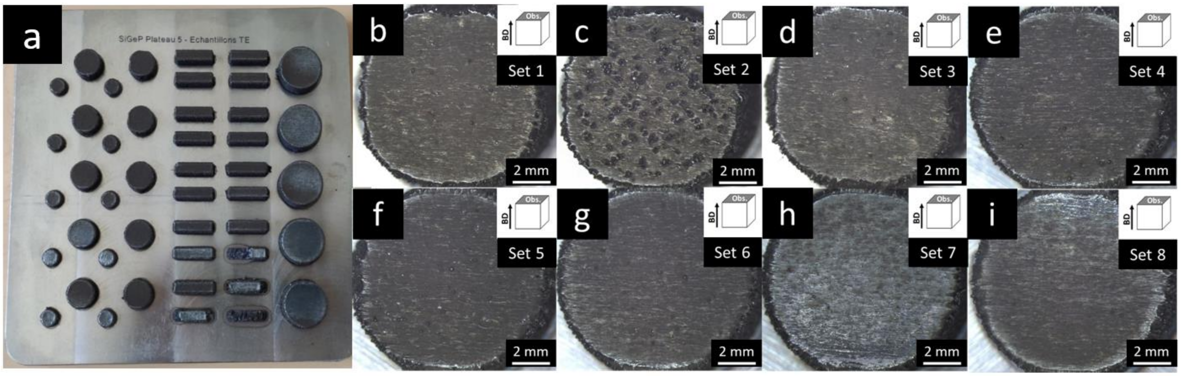

Figure 4. Pictures of as built tray and samples. Figure 4a display a photo of tray 2. Figure 4b-i correspond to binocular top view of as built shape 2 samples printed with printing parameters set 1-8 respectively.

Table 6. Printing quality relative to samples shapes, dimensions and printing parameters.

Tray 1		Section	Height	General aspect Set 1	General aspect Set 2	General aspect Set 3
Shape 1	Cylinder	d=5.2mm	5mm	Partially crumbled	Partially crumbled	Completely built
Shape 2	Cylinder	d=9.8mm	7mm	Completely built	Completely built	Completely built
Shape 3	Cuboid	3x15mm^2	7mm	Crumbled	Partially crumbled	Completely built
				Completely built	Completely built	Completely built
Shape 4	Cuboid	5x5mm^2	7mm	Crumbled	Crumbled	Completely built
Shape 5	Cuboid	10x10mm^2	14mm	Partially crumbled	Completely built	Completely built
Shape 6	Cuboid	3x3mm^2	14mm	Teared off	Teared off	Crumbled

Tray 2		Section	Height	General aspect Set 4	General aspect Set 5	General aspect Set 6	General aspect Set 7	General aspect Set 8
Shape 1	Cylinder	d=5.2mm	3mm	Completely built	Completely built	Completely built	Completely built	Completely built
				Completely built	Completely built	Completely built	Completely built	Completely built
Shape 2	Cylinder	d=9.8mm	5mm	Completely built	Completely built	Completely built	Completely built	Completely built
				Completely built	Completely built	Completely built	Completely built	Completely built
Shape 3	Cuboid	3x15mm^2	5mm	Completely built	Completely built	Completely built	Completely built	Completely built
				Completely built	Completely built	Completely built	Completely built	Crumbled
				Completely built	Completely built	Completely built	Partially crumbled	Crumbled
				Completely built	Completely built	Completely built	Crumbled	Teared off
Shape 7	Cylinder	d=14mm	7mm	Completely built	Completely built	Completely built	Completely built	Completely built

2.3. Sample preparation

All samples were removed from the tray via localized shock. Samples studied by optical microscopy were coated with epoxy and polished with a PRESI Mecatech 234 disc polisher and colloidal silica. Samples studied by SEM were coated with a composite carbon black/phenol and polished with colloidal silica. SEM images and EDS analysis were conducted on a LEO 1530 SEM, and EBSD analysis was conducted on a Zeiss Merlin FE-SEM.

3. Results and discussion

3.1. Density

Shape 5 and 7 samples density was measured by Archimedes method [33] with a Mettler balance (Type AE200) for all printing parameters sets. The fluid used is anhydrous ethanol. Table 7 displays measured densities and open porosity, along parts density and closed porosity, calculated relative to powder pycnometer density (3.107g.cm^{-3}).

Table 7. Density and open porosity measured on shape 5 and 7 samples by Archimedes methods. Closed porosity and parts density are calculated relative to measured powder pycnometer density.

	Set 1	Set 2	Set 3	Set 4	Set 5	Set 6	Set 7	Set 8
Density (g.cm^{-3})	2.99	2.85	3.00	2.95	2.98	3.00	2.97	2.96
Open porosity (%)	0.8	5.4	0.5	1.9	0.9	0.8	1.2	1.8
Closed porosity (%)	2.9	2.8	3.0	3.3	3.1	2.6	3.1	2.9
% of pycnometer density	96.4	91.8	96.5	94.8	96.0	96.6	95.7	95.3

Part densities are between 91.8% and 96.6% of powder density, with a calculated amount of closed porosity of 3%. Figure 5 shows measured densities relative to *VED*. Set 2's point displays the lowest density for the lowest *VED* value. This sample presents columnar lack of fusion defects, which explains the low densities observed. Samples from set 1, 3, 5 and 6 are above 96% of theoretical density. These four sets are within *VED* between 140 and 220 J.mm^{-3}.

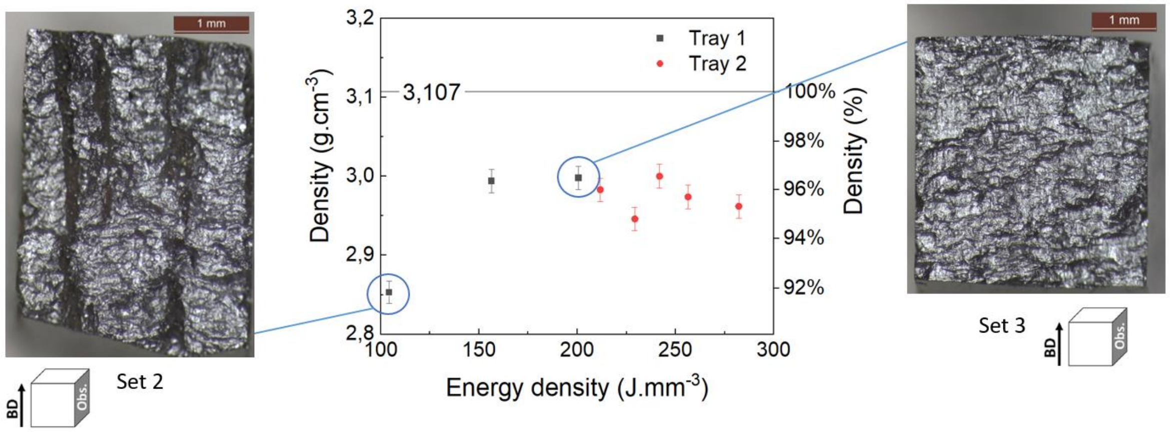

Figure 5. Density measured by Archimedes method relative to VED. Density was measured on shape 5 samples in tray 1 and shape 7 samples in tray 2. The horizontal line displays powder pycnometer density, which was used as reference.

An optical analysis was conducted on sample cuts along BD, to gather more information on porosities. Two samples were studied: set 1 shape 5 (three cut planes) and set 6 shape 7 (four cut planes). Table 8 displays densities measured by optical analysis. On set 1 shape 5 sample, relative density measured with optical analysis is equal to the one obtained by Archimedes method. However, Set 6 shape 7 sample's density measured with optical analysis is slightly higher than its density obtained with Archimedes method.

Table 8. Density of set 1 shape 5 and set 6 shape 7 samples measured by optical analysis.

Density (%)	Cut plane 1	Cut plane 2	Cut plane 3	Cut plane 4	Mean
Set 1 shape 5	96.3	95.8	97.2	/	96.4
Set 6 shape 7	97.5	97.8	97.6	97.8	97.7

Figure 6 displays optical microscope images of set 6 shape 7 sample. Figure 6 b) highlights a high number of cracks, aligned in two directions: parallel and perpendicular to BD. As displayed in Figure 6 c), these cracks tend to intersect each other, and intersect porosities, which limits their identification by the software.

Defects circle equivalent (CE) diameter, aspect ratio and orientation relative to horizontal plane (with BD=90°) were measured on cut planes with Leica Application Suite X software (Figure 7). CE diameter follows a Gaussian repartition centred around 3µm. Aspect ratio curves display two peaks: one at 0.2, and a smaller one around 0.8. The 0.2 peak corresponds to the high number of cracks observed in Figure 6 c). The smaller peak around 0.8 aspect ratio is attributed to circular pores observed throughout samples. Defects orientation is more equally distributed, probably due to intersecting defects. Two preferential orientations are observed, at circa 80° and 25°, and those peaks are mirrored relative to 90° orientation. These peaks could be attributed to cracks alignment observed on Figure 6 b).

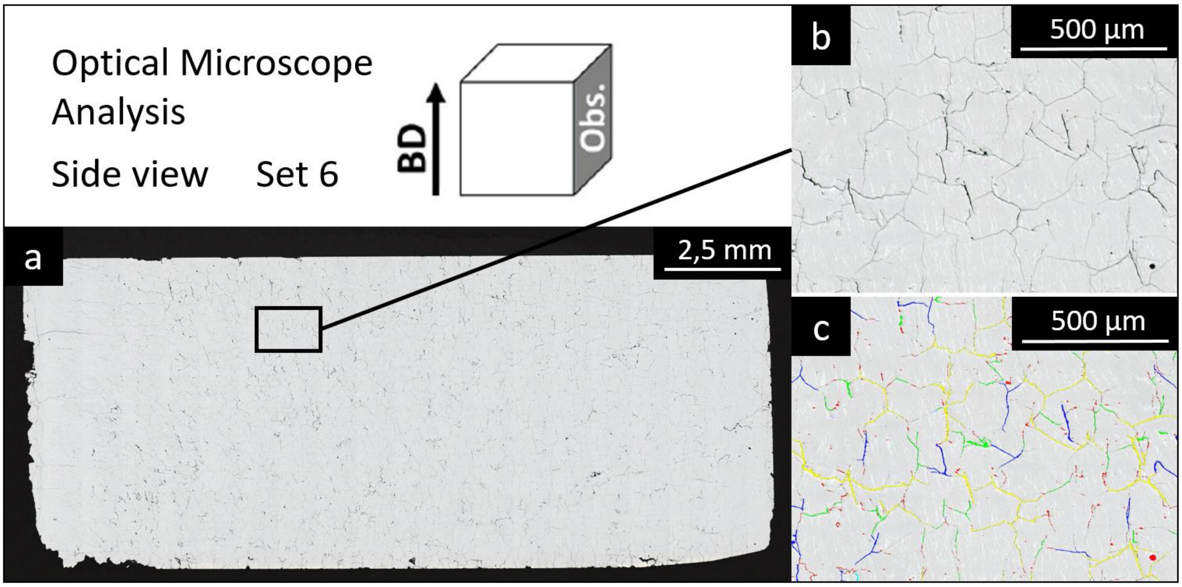

Figure 6. Optical microscope analysis of shape 7 set 6 sample cut along BD. Figure 6a shows an optical microscope composite image of all sample’s cut plane. Figure 6 b is a zoomed image of figure a, and Figure 6 c shows porosities detection by Leica Application Suite X software.

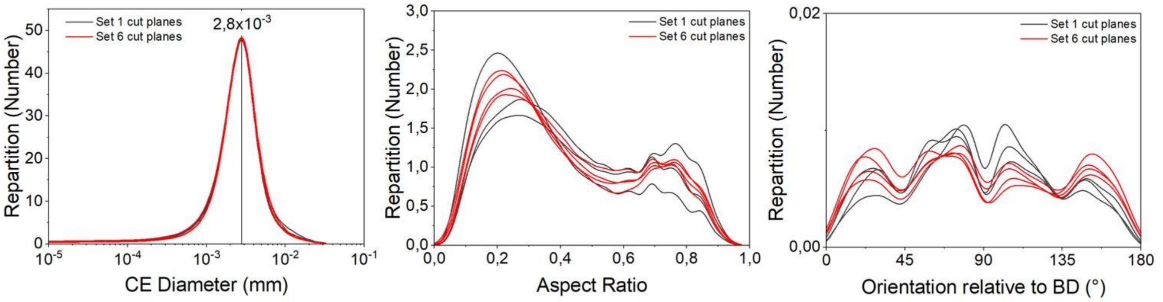

Figure 7. Defects CE diameter, aspect ratio and orientation relative to horizontal plane (with BD = 90°) measured on samples set 1 shape 5 and set 6 shape 7 cut planes with Leica Application Suite X software.

3.2. Chemical composition

Table 9 presents set 6 shape 2 sample ICP-OES chemical analysis results. The atomic percentage of silicon and germanium does not vary significantly. However, the amount of phosphorus in the sample (0.8at%) is 33% inferior to its initial amount in the powder (1.2at%), due to its vaporization during the manufacturing process. Drops in phosphorus concentration are also encountered in atomisation[34], hot pressing[2,35], and other processes[36]. In all of these processes, phosphorus losses are compensated by increasing base material phosphorus content relative to target composition. More broadly, element vaporisation was also observed with other thermoelectric materials processed by L-PBF due to the high temperatures reached by the melt pool [16].

Table 9. Chemical composition of set 6 shape 2 sample measured par ICP-OES. Last column shows powder chemical composition for comparison.

Atomic element	weight %	weight % uncertainty	atomic %	atomic % uncertainty	atomic % (powder)
Silicon	60	3	79	2	79
Germanium	40	2	20	2	20
Phosphorus	0,6	0.1	0.8	0.1	1.2

3.3. Microstructure

Figure 8 shows SEM images of set 5 shape 3 sample. On these pictures, dark structures with a bright outline are visible. These structures are columnar-shaped and aligned along BD (Figure 8b). Anisotropic microstructure along BD is common in AM, as in most of the cases, thermal gradient, which drives solidification process, is oriented along this direction. In perpendicular plan relative to BD (Figure 8a), some structures are locally aligned with their neighbours, however no preferential direction is observed on macroscopic scale. The average area of these structures was measured on Figure 8 a with ImageJ. The CE diameter of these structures average area is 8µm. These structures are observed on samples from all sets, with no major difference between sets. Finally, cracks are visible on both images, and were observed on all samples; they are discussed on part 3.4.

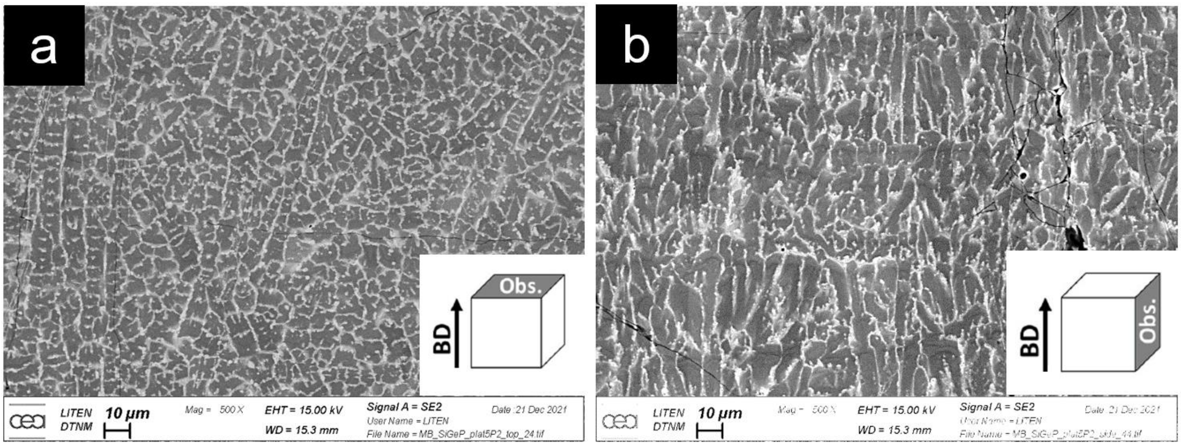

Figure 8. SEM images of set 5 shape 3 sample with a x500 magnification. Figure 8a and 8b correspond to sample top and side views, respectively.

To investigate the nature of these structures, an Electron Backscatter Diffraction (EBSD) analysis was conducted on a set 8 shape 3 sample side view (Figure 9). Figure 9a displays grain boundaries with the image quality (IQ) map. Grain boundaries are identified by local disorientation observed in inverse pole figures. They are classified in three categories: low angle grain boundaries (misorientation from 5° to 15°), high angle grain boundaries (misorientation from 15° to 59°), and Coincident Site Lattice (CSL) Σ3 (misorientation from 59° to 61°). SiGe displays a high number of CSL Σ3 grain boundaries, which was also observed in EBSD analysis of SiGe thin films [37]. Grains identified with EBSD are larger than structures observed in Figure 9c, which suggest that these are substructures within grains. Substructures within grains are common in L-PBF, as cellular[38] and dendritic[32,39] microstructures.

Figure 9b presents an inverse pole figure map along BD. Orientations close to [101] and [111] plans families are more represented within this image. Preferential growth for SiGe diamond structures is [101][40]. The high representation of [101] orientations in figure 9b confirms that preferential growth happen along BD. In L-PBF, grains aligned along melt pool shapes are common, however such alignment are not visible in Figure 9b, which suggest that grain formation follows through different melt pools. Finally, large grains close to [111] orientation are observed on the top right of the image. When observed in figure 9c, these grains present substructures parallel to each other, which suggest that these substructures are dendritic arms.

An Energy-Dispersive X-ray Spectroscopy (EDS) map was conducted on a set 6 shape 3 sample top view (Figure 10). Silicon and germanium repartition within material is inhomogeneous, with micro-segregation of germanium observed at substructures boundaries. SiGe solidus temperature decreases with Ge concentration. Solidification structures with higher Si content form first, as their solidification temperature is higher. As they grow, Si content in the liquid phase diminishes, and solidifies at the end in a Ge-rich phase at substructure boundaries. This phenomenon occurs also in other forming processes [27,37,41]. Such disparities in element concentration are expected to limit TE performances as it alters locally the band gap, and increases locally scattering sites [27]. Phosphorus tends also to group in cluster at substructure boundaries, with a similar mechanism, limiting its doping effect [42,43]. In response to this, annealing and activation annealing are usually performed to homogenize elements concentration[44].

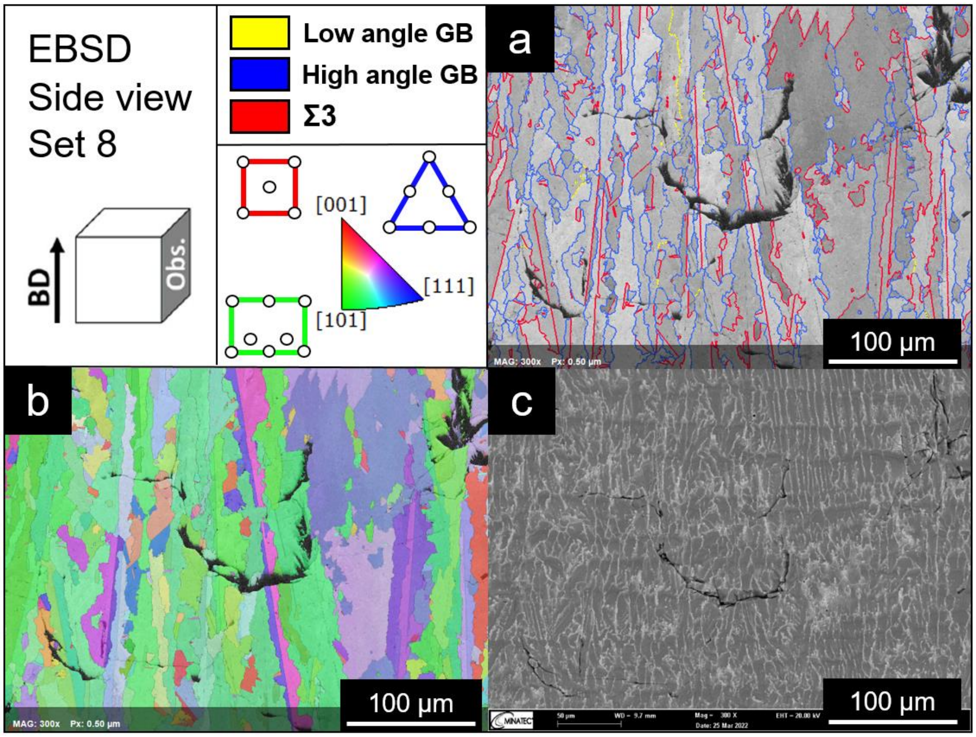

Figure 9. EBSD analysis of set 8 shape 3 sample side view. Figure 9a displays grain boundaries with IQ map, Figure 9b an inverse pole figure map along BD and Figure 9c a BSD image of studied zone.

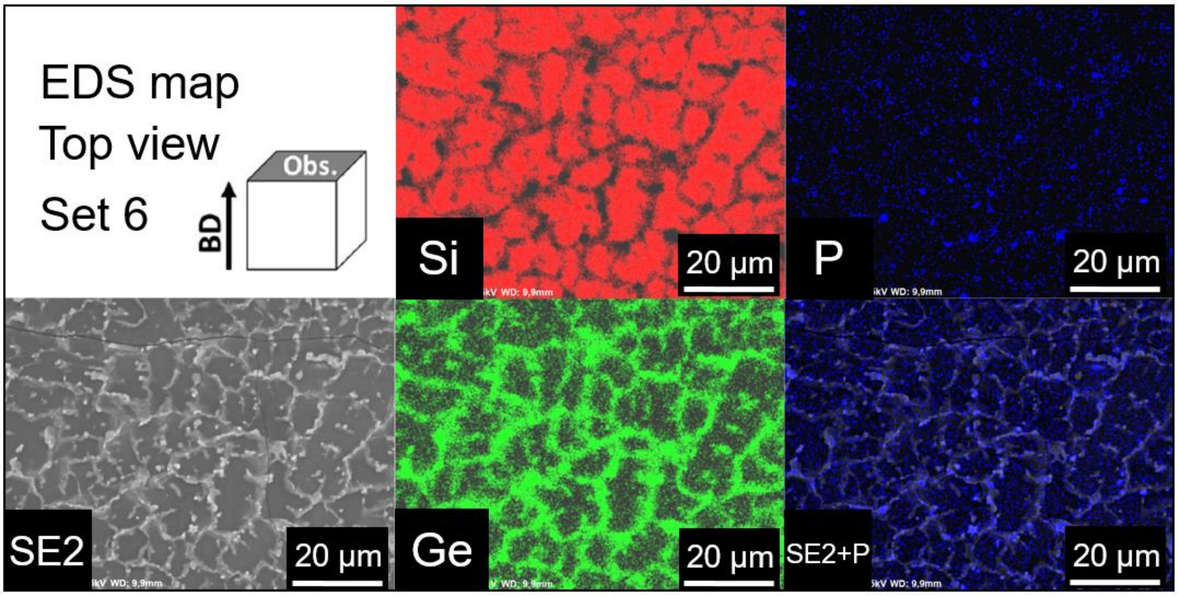

Fig 10. EDS map of a set 6 shape 3 sample top view.

3.4. Cracks analysis

Figure 11 shows binocular, optical microscope and SEM images of printed samples. All printed samples present cracks. In samples top views, cracks tend to be aligned with laser tracks direction, as presented in Figure 11a and 11b. Inter-crack distance was measured on optical microscope top view images for tray 1's sets (Table 11). Shape 3 and 5 samples were investigated. Mean inter-crack distance measured ranges from 100 to 150 µm, with no significant difference observed between sets or between the two samples types. This size corresponds to single tracks width measured on printing quality map tray (respectively 117, 102 and 138µm for set 1, 2 and 3). Figures 11c and 11d display side view of samples, with samples observed parallel to BD. From this view, cracks are semi-circular shaped, with a size ranging from 70 to 150µm. Cracks shape and size suggest that crack propagation tend to follow melt pool shape, resulting in semi-circular cracks in side views and cracks aligned with laser tracks in top views.

Table 11. Mean inter-cracks distance measured on top view of tray 1 shape 3 and 5 samples.

Sample shape	Parameter set	mean inter-crack distance (µm)	standard deviation (µm)
Shape 3	Set 1	126	35
	Set 2	117	25
	Set 3	159	23
Shape 5	Set 1	107	16
	Set 2	117	17
	Set 3	117	14

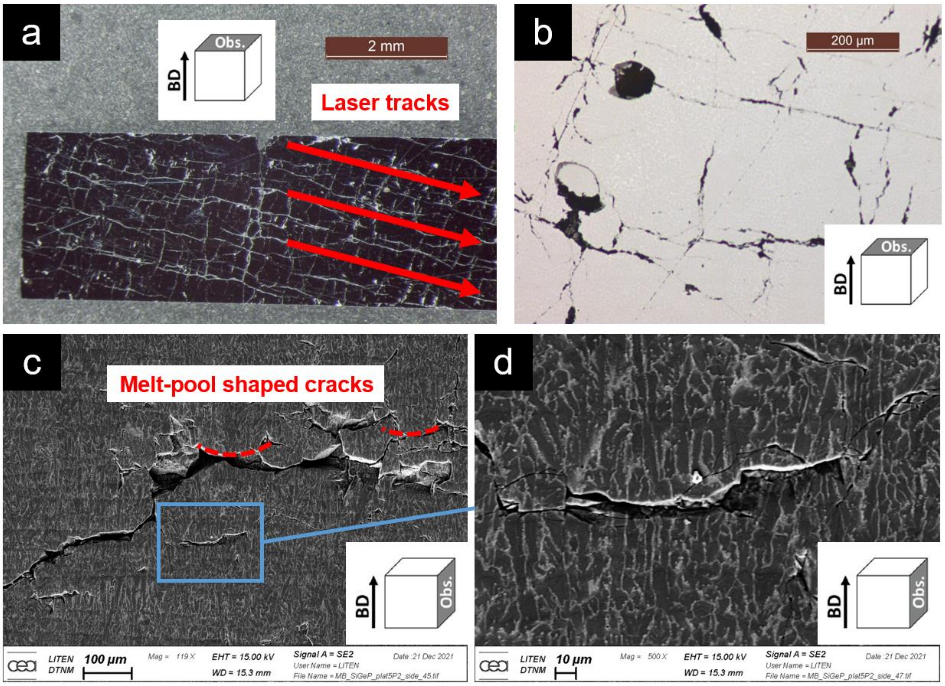

Figure 11. Images of printed samples. Figure 11a shows a top-view binocular image of set 1 shape 3 sample. Figure 11b shows a top-view optical microscope image of set 1 shape 3 sample. Figure 11c and 11d show a side-view SEM image of set 5 shape 3 sample cracks.

Figure 11d highlights a transgranular fracture mode, with cracks crossing substructures independently of their boundaries. The same phenomenon is observed Figure 9 for grain boundaries, which indicates that cracking happen after grain formation. This implies that cracks observed here are not due to hot cracking[45] but corresponds more to solid state thermal induced cracking, likely caused by the high thermal gradients encountered in melt pool periphery[46]. Although SiGe thermal expansion coefficient (3.11x10^{-6} K^{-1}) is inferior to metals (circa 20x10^{-6} K^{-1}), SiGe is also more brittle than metals, which can further support this hypothesis [4,5]. Cracking was also observed in a lesser extent with other TE materials L-PBF processing [6,7,11].

3.5. Thermoelectric properties

Figure 12 presents the temperature dependence of TE properties measured on tray 1 sets. As each characterisation tool needs samples of specific shape and sizes, TE properties are measured on different samples printed with the same parameters set. They are compared to typical properties obtained for n-type sintered SiGe [2].

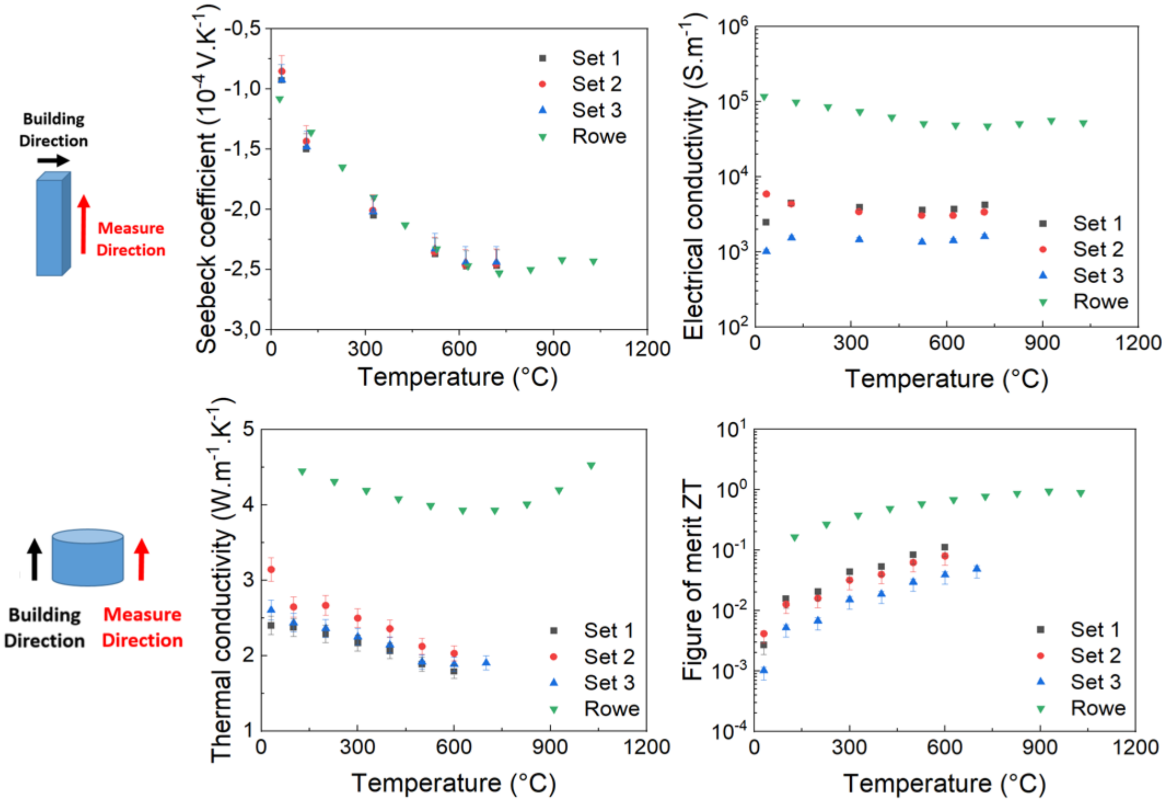

Figure 12. Temperature dependence of thermoelectric properties measured on tray 1 samples and of sintered N-type SiGe [Rowe, 1995][2].

Seebeck coefficient and electric conductivity were measured on shape 3 samples, perpendicular to BD, via four-probe method with ZEM3 machine from ULVAC©. Seebeck coefficient values are close to Rowe's work, and no significant difference was observed between Seebeck coefficients for the three parameters sets. However, electrical conductivity values are one decade below usual values obtained for SiGe. Electrical conductivity of set 3 sample is lower than electrical conductivities of the two other sets. The high number of cracks can explain low electrical conductivities. Ge content inhomogeneity within the grains can also create scattering sites for electrons as lattice constant depends on Ge content in SiGe [47], and those differences in lattice constant are likely to produce intra-granular defects. Finally, EDS analyses showed that phosphorus repartition is inhomogeneous throughout the material, which can reduce the dopant role in enhancing electric conductivity of the material.

Thermal conductivity κ can be expressed as the product of density ρ, thermal diffusivity α and specific heat C_p, as in equation 5:

$$\kappa = C_p \, \alpha \, \rho \tag{5}$$

Thermal conductivities presented in this work are the product of three separate measures of respectively density, thermal diffusivity and specific heat. Specific heat was measured on shape 1 samples, perpendicular to BD, with a thermo-gravimetric analyser STA 449 F3/F1 Jupiter from NETZCH©. Thermal diffusivity was measured on shape 2 samples, parallel to BD, with a diffusimeter LFA 457 from NETZCH©. Specific heat and thermal diffusivity were measured relative to temperature whereas density is considered constant in regards to temperature variation.

Thermal conductivities obtained in this work are advantageously lower from Rowe's by a factor two, with a gap of $2 W.m^{-1}.K^{-1}$ between Rowe and this work. Thermal conductivity can be viewed as the sum of phonon contribution κ_p and electron contribution κ_e ($\kappa = \kappa_p + \kappa_e$). With Wiedemann-Franz law, κ_e can be estimated with electrical conductivities values thanks to equation 6:

$$\kappa_e = L_0 \, \sigma \, T \tag{6}$$

with L_0 the Lorentz number, σ the electrical conductivity, and T the temperature. The gap of κ_e between Rowe and this work calculated with electrical conductivities values is circa $1 W.m^{-1}.K^{-1}$, which suggest that κ_p of samples from this work is inferior to Rowe's. Cracks and defects observed throughout the material can explain this lower κ_p.

Finally, figure of merit obtained in this work are approximately one decade behind reference values for SiGe. The one decade gap observed while measuring electrical conductivities carries over to ZT diagram. Interestingly, set 3 presents the weakest ZT whereas it was the most effective set of the three in regards to printing quality. Maximum ZT values for sets 1, 2 and 3 are respectively 0.11, 0.07 and 0.04 at 600°C.

4. Conclusion and perspectives

In this work, N-type SiGe bulk materials were synthesized for the first time by L-PBF process, from a non-optimized N-SiGe powder. Printing parameters were investigated, and four parameter sets successfully produced dense samples of various shapes. Some of printed samples displays densities superior to 96% of powder pycnometer density, which proves the process capability to produce SiGe parts with good density. However, all samples present cracks that are likely to be caused by high thermal gradients induced in the material during the printing process.

TE properties were investigated, with a peak *ZT* value of 0.11 at 600°C obtained with set 1 samples. Electrical conductivities measured in this work are one decade below usual values for bulk SiGe-P samples processed by other methods, showing that further improvement has still to be made to enhance carrier mobility within the material. Cracks and micro-segregation observed within samples are likely to act as scattering site for electrons, and could explain the low electrical conductivities measured.

Further work needs to be performed to avoid these two phenomena. For instance, cracking in L-PBF can be limited by reducing thermal gradient with a high temperature heating plate, or with additional laser scanning. It is known that nanostructured SiGe shows better mechanical and TE performance than regular SiGe alloy[48]. Nucleating agents could help reduce grain size, and distribute stress in more grain boundaries, which may reduce cracking. Finally, annealing can help reduce micro-segregation by diffusing elements from grain boundaries to the center. Overall, these results are promising for SiGe bulk manufacturability by L-PBF process, which can open up its scope of applications by introducing new geometries and limiting material losses.

Acknowledgments

We would like to thanks Camille Flament, Celine Ribière, Bastien Marchais, Pascal Faucherand and Jean Leforestier for their respective contributions to this work, namely EBSD analysis, powder analysis, part manufacturing, sample observation and characterisation. This work would not have been possible without their implication and their expertise.

Data Availability

The data that support the findings of this study are available from the corresponding author, Maxime Baudry, upon reasonable request.

References

[1] D. Champier, Générateurs thermoélectriques : de la conception aux applications, Conversion de l'énergie électrique. (2018). https://doi.org/10.51257/a-v1-d3241.

[2] D.M. Rowe, ed., CRC handbook of thermoelectrics, CRC Press, Boca Raton, FL, 1995.

[3] R. He, G. Schierning, K. Nielsch, Thermoelectric Devices: A Review of Devices, Architectures, and Contact Optimization, Adv. Mater. Technol. 3 (2018) 1700256. https://doi.org/10.1002/admt.201700256.

[4] S. Bathula, B. Gahtori, J. Mula, S.K. Tripathy, K. Tyagi, A. Srivastava, A. Dhar, Microstructure and mechanical properties of thermoelectric nanostructured n-type silicon-germanium alloys synthesized employing spark plasma sintering, Applied Physics Letters. 105 (2014) 061902–061902. https://doi.org/10.1063/1.4892879.

[5] A.C. Kallel, G. Roux, C.L. Martin, Thermoelectric and mechanical properties of a hot pressed nanostructured n-type Si80Ge20 alloy, Materials Science and Engineering: A. 564 (2013) 65–70. https://doi.org/10.1016/j.msea.2012.11.073.

[6] A. El-Desouky, M. Carter, M.A. Andre, P.M. Bardet, S. LeBlanc, Rapid processing and assembly of semiconductor thermoelectric materials for energy conversion devices, Materials Letters. 185 (2016) 598–602. https://doi.org/10.1016/j.matlet.2016.07.152.

[7] A. El-Desouky, M. Carter, M. Mahmoudi, A. Elwany, S. LeBlanc, Influences of energy density on microstructure and

consolidation of selective laser melted bismuth telluride thermoelectric powder, Journal of Manufacturing Processes. 25 (2017) 411–417. https://doi.org/10.1016/j.jmapro.2016.12.008.

[8] H. Zhang, D. Hobbis, G.S. Nolas, S. LeBlanc, Laser additive manufacturing of powdered bismuth telluride, Journal of Materials Research. 33 (2018) 4031–4039. https://doi.org/10.1557/jmr.2018.390.

[9] Y. Du, J. Chen, Q. Meng, J. Xu, B. Paul, P. Eklund, Flexible ternary carbon black/Bi2Te3 based alloy/polylactic acid thermoelectric composites fabricated by additive manufacturing, Journal of Materiomics. 6 (2020) 293–299. https://doi.org/10.1016/j.jmat.2020.02.010.

[10] Y. Du, J. Chen, Q. Meng, Y. Dou, J. Xu, S.Z. Shen, Thermoelectric materials and devices fabricated by additive manufacturing, Vacuum. 178 (2020) 109384. https://doi.org/10.1016/j.vacuum.2020.109384.

[11] A. El-Desouky, A. Read, P. Bardet, M. Andre, S. Leblanc, Selective laser melting of a bismuth telluride thermoelectric material, Proc. Solid Free. Symp. (2015) 1043–1050.

[12] M.J. Carter, A. El-Desouky, M.A. Andre, P. Bardet, S. LeBlanc, Pulsed laser melting of bismuth telluride thermoelectric materials, Journal of Manufacturing Processes. 43 (2019) 35–46. https://doi.org/10.1016/j.jmapro.2019.04.021.

[13] J. Qiu, Y. Yan, T. Luo, K. Tang, L. Yao, J. Zhang, M. Zhang, X. Su, G. Tan, H. Xie, M.G. Kanatzidis, C. Uher, X. Tang, 3D Printing of highly textured bulk thermoelectric materials: mechanically robust BiSbTe alloys with superior performance, Energy Environ. Sci. 12 (2019) 3106–3117. https://doi.org/10.1039/C9EE02044F.

[14] J. Shi, H. Chen, S. Jia, W. Wang, 3D printing fabrication of porous bismuth antimony telluride and study of the thermoelectric properties, Journal of Manufacturing Processes. 37 (2019) 370–375. https://doi.org/10.1016/j.jmapro.2018.11.001.

[15] R. Welch, D. Hobbis, A.J. Birnbaum, G. Nolas, S. LeBlanc, Nano- and Micro-Structures Formed during Laser Processing of Selenium Doped Bismuth Telluride, Advanced Materials Interfaces. 8 (2021) 2100185. https://doi.org/10.1002/admi.202100185.

[16] Y. Mao, Y. Yan, K. Wu, H. Xie, Z. Xiu, J. Yang, Q. Zhang, C. Uher, X. Tang, Non-equilibrium synthesis and characterization of n-type Bi2Te2.7Se0.3 thermoelectric material prepared by rapid laser melting and solidification, RSC Adv. 7 (2017) 21439–21445. https://doi.org/10.1039/C7RA02677C.

[17] K. Wu, Y. Yan, J. Zhang, Y. Mao, H. Xie, J. Yang, Q. Zhang, C. Uher, X. Tang, Preparation of n-type Bi2Te3 thermoelectric materials by non-contact dispenser printing combined with selective laser melting, Physica Status Solidi (RRL) – Rapid Research Letters. 11 (2017) 1700067. https://doi.org/10.1002/pssr.201700067.

[18] R. Zhan, J. Lyu, D. Yang, Y. Liu, S. Hua, Z. Xu, C. Wang, X. Peng, Y. Yan, X. Tang, Large-scale SHS based 3D printing of high-performance n-type BiTeSe: Comprehensive development from materials to modules, Materials Today Physics. 24 (2022) 100670. https://doi.org/10.1016/j.mtphys.2022.100670.

[19] J. Shi, X. Chen, W. Wang, H. Chen, A new rapid synthesis of thermoelectric Sb2Te3 ingots using selective laser melting 3D printing, Materials Science in Semiconductor Processing. 123 (2021) 105551. https://doi.org/10.1016/j.mssp.2020.105551.

[20] Y. Thimont, L. Presmanes, V. Baylac, P. Tailhades, D. Berthebaud, F. Gascoin, Thermoelectric Higher Manganese Silicide: Synthetized, sintered and shaped simultaneously by selective laser sintering/Melting additive manufacturing technique, Materials Letters. 214 (2018) 236–239. https://doi.org/10.1016/j.matlet.2017.12.026.

[21] Y. Wu, K. Sun, S. Yu, L. Zuo, Modeling the selective laser melting-based additive manufacturing of thermoelectric powders, Additive Manufacturing. 37 (2021) 101666. https://doi.org/10.1016/j.addma.2020.101666.

[22] J. Lee, S. Choo, H. Ju, J. Hong, S.E. Yang, F. Kim, D.H. Gu, J. Jang, G. Kim, S. Ahn, J.E. Lee, S.Y. Kim, H.G. Chae, J.S. Son, Doping-Induced Viscoelasticity in PbTe Thermoelectric Inks for 3D Printing of Power-Generating Tubes, Advanced Energy Materials. 11 (2021) 2100190. https://doi.org/10.1002/aenm.202100190.

[23] F. Laverne, F. Segonds, P. Dubois, Fabrication additive - Principes généraux, Conception et Production. (2016). https://doi.org/10.51257/a-v2-bm7017.

[24] S. Pillot, Fusion laser sélective de lit de poudres métalliques, Travail des matériaux - Assemblage. (2016). https://doi.org/10.51257/a-v1-bm7900.

[25] I. Yadroitsev, Selective laser melting, LAP LAMBERT Academic Publishing, 2009. https://www.morebooks.shop/store/gb/book/selective-laser-melting/isbn/978-3-8383-1794-6 (accessed January 4, 2022).

[26] H.R. Kotadia, G. Gibbons, A. Das, P.D. Howes, A review of Laser Powder Bed Fusion Additive Manufacturing of aluminium alloys: Microstructure and properties, Additive Manufacturing. 46 (2021) 102155. https://doi.org/10.1016/j.addma.2021.102155.

[27] N. Hussain, A.M. Mullis, N. Haque, Effect of cooling rate on the microstructure of rapidly solidified SiGe, Materials Characterization. 154 (2019) 377–385. https://doi.org/10.1016/j.matchar.2019.06.014.

[28] M.A. Spurek, L. Haferkamp, C. Weiss, A.B. Spierings, J.H. Schleifenbaum, K. Wegener, Influence of the particle size distribution of monomodal 316L powder on its flowability and processability in powder bed fusion, Prog Addit Manuf. (2021). https://doi.org/10.1007/s40964-021-00240-z.

[29] R.L. Carr, Evaluating Flow Properties of Solids, Chemical Engineering Journal. (1965) 163–168.

[30] N. Batista, J. Crandall, A. El Desouky, S. LeBlanc, S. Wang, J. Yang, Powder Metallurgy Characterization of Thermoelectric Materials for Selective Laser Melting, TechConnect Briefs. 4 (2017) 166–169.

[31] M.E. Levinshteĭn, S.L. Rumyantsev, M. Shur, eds., Properties of advanced semiconductor materials: GaN, AlN, InN, BN, SiC, SiGe, Wiley, New York, 2001.

[32] H.R. Javidrad, S. Salemi, Effect of the Volume Energy Density and Heat Treatment on the Defect, Microstructure, and Hardness of L-PBF Inconel 625, Metall Mater Trans A. 51 (2020) 5880–5891. https://doi.org/10.1007/s11661-020-05992-x.

[33] A.B. Spierings, M. Schneider, R. Eggenberger, Comparison of density measurement techniques for additive manufactured metallic parts, Rapid Prototyping Journal. 17 (2011) 380–386. https://doi.org/10.1108/13552541111156504.

[34] M. Otake, K. Sato, O. Sugiyama, S. Kaneko, Effect of Ball-Milling on Sinterability of SiGe Powders Prepared by Gas Atomization of the Corresponding Melts, Journal of The Ceramic Society of Japan - J CERAMIC SOC JPN. 111 (2003) 749–754. https://doi.org/10.2109/jcersj.111.749.

[35] J.L. Harringa, B.A. Cook, Application of hot isostatic pressing for consolidation of n-type silicon–germanium alloys prepared by mechanical alloying, Materials Science and Engineering: B. 60 (1999) 137–142. https://doi.org/10.1016/S0921-5107(99)00023-9.

[36] D. Thompson, D. Hitchcock, A. Lahwal, T.M. Tritt, Single-element spark plasma sintering of silicon germanium, Emerging Materials Research. 1 (2012) 299–305. https://doi.org/10.1680/emr.12.00019.

[37] G. Sison, P. Chiang, C. Lan, Growth of polycrystalline Si0.7Ge0.3 on various substrates for thermoelectric applications, Journal of Crystal Growth. 585 (2022) 126599. https://doi.org/10.1016/j.jcrysgro.2022.126599.

[38] K.G. Prashanth, J. Eckert, Formation of metastable cellular microstructures in selective laser melted alloys, Journal of Alloys and Compounds. 707 (2017) 27–34. https://doi.org/10.1016/j.jallcom.2016.12.209.

[39] S. Paul, J. Liu, S.T. Strayer, Y. Zhao, S. Sridar, M.A. Klecka, W. Xiong, A.C. To, A Discrete Dendrite Dynamics Model for Epitaxial Columnar Grain Growth in Metal Additive Manufacturing with Application to Inconel, Additive Manufacturing. 36 (2020) 101611. https://doi.org/10.1016/j.addma.2020.101611.

[40] Y. Azuma, N. Usami, K. Fujiwara, T. Ujihara, K. Nakajima, A simple approach to determine preferential growth orientation using multiple seed crystals with random orientations and its utilization for seed optimization to restrain polycrystallization of SiGe bulk crystal, Journal of Crystal Growth. 276 (2005) 393–400. https://doi.org/10.1016/j.jcrysgro.2004.11.430.

[41] S. Wongprakarn, S. Pinitsoontorn, S. Tanusilp, K. Kurosaki, Enhancing thermoelectric properties of p-type SiGe alloy through optimization of carrier concentration and processing parameters, Materials Science in Semiconductor Processing. 88 (2018) 239–249. https://doi.org/10.1016/j.mssp.2018.08.020.

[42] A. Pakfar, Dopant diffusion in SiGe: modeling stress and Ge chemical effects, Materials Science and Engineering: B. 89 (2002) 225–228. https://doi.org/10.1016/S0921-5107(01)00790-5.

[43] A. Chroneos, H. Bracht, R.W. Grimes, B.P. Uberuaga, Phosphorous clustering in germanium-rich silicon germanium, Materials Science and Engineering: B. 154–155 (2008) 72–75. https://doi.org/10.1016/j.mseb.2008.08.005.

[44] T.-C. Kuo, K.-J. Jhong, C.-W. Lin, W.-H. Lee, Effect of annealing conditions on dopants activation and stress conservation in silicon-germanium, AIP Advances. 9 (2019) 015110. https://doi.org/10.1063/1.5053237.

[45] M. Opprecht, J.-P. Garandet, G. Roux, C. Flament, M. Soulier, A solution to the hot cracking problem for aluminium alloys manufactured by laser beam melting, Acta Materialia. 197 (2020) 40–53. https://doi.org/10.1016/j.actamat.2020.07.015.

[46] A. Mostafaei, C. Zhao, Y. He, S. Reza Ghiaasiaan, B. Shi, S. Shao, N. Shamsaei, Z. Wu, N. Kouraytem, T. Sun, J. Pauza, J.V. Gordon, B. Webler, N.D. Parab, M. Asherloo, Q. Guo, L. Chen, A.D. Rollett, Defects and anomalies in powder bed fusion metal additive manufacturing, Current Opinion in Solid State and Materials Science. 26 (2022) 100974. https://doi.org/10.1016/j.cossms.2021.100974.

[47] J.P. Dismukes, L. Ekstrom, E.F. Steigmeier, I. Kudman, D.S. Beers, Thermal and Electrical Properties of Heavily Doped Ge-Si Alloys up to 1300°K, Journal of Applied Physics. 35 (1964) 2899–2907. https://doi.org/10.1063/1.1713126.

[48] H. Lee, D. Vashaee, D.Z. Wang, M.S. Dresselhaus, Z.F. Ren, G. Chen, Effects of nanoscale porosity on thermoelectric properties of SiGe, Journal of Applied Physics. 107 (2010) 094308. https://doi.org/10.1063/1.3388076.